nature communications

Article

https://doi.org/10.1038/s41467-025-58709-2

Revealing the structure-activity relationship of Pt_1/CeO_2 with ^{17}O solid-state NMR spectroscopy and DFT calculations

Received: 11 August 2024

Accepted: 28 March 2025

Published online: 14 April 2025

Check for updates

Yujie Wen[1,14], Fang Wang[1,14], Jie Zhu[2,3], Qian Wen[4], Xiaoli Xia[1], Juan Wen[1], Changshun Deng[1], Jia-Huan Du[5], Xiaokang Ke[1], Zhen Zhang[4,6], Hanxi Guan[7], Lei Nie[8,9], Meng Wang[10], Wenhua Hou[1], Wei Li[1], Weiping Tang[11], Weiping Ding[1], Junchao Chen[11] ✉ & Luming Peng[1,12,13] ✉

Single-atom catalysts (SACs) have attracted significant interest due to their exceptional and tunable performance, enabled by diverse coordination environments achieved through innovative synthetic strategies. However, various local structures of active sites pose significant challenges for precise characterization, a prerequisite for developing structure-activity relationships. Here, we combine ^{17}O solid-state NMR spectroscopy and DFT calculations to elucidate the detailed structural information of Pt/CeO_2 SACs and their catalytic behaviors. The NMR data reveal that single Pt atoms, dispersed from clusters with water vapor, exhibit a square planar geometry embedded in CeO_2 (111) surface, distinct from the original clusters and other conventionally generated Pt single atoms. The square planar Pt/CeO_2 SAC demonstrates improved CO oxidation performance compared to Pt/CeO_2 SAC with octahedral coordination, due to moderately strong CO adsorption and low energy barriers. This approach can be extended to other oxide-supported SACs, enabling spatially resolved characterization and offering comprehensive insights into their structure-activity relationships.

Single-atom catalysts (SACs) are increasingly recognized for their pivotal role in catalysis due to their maximized atomic economy (especially for noble metals), superior catalytic activity, and selectivity[1–6]. By employing tailored synthesis strategies[7], oxide-supported SACs can achieve tunable active sites resulting from the distinct spatial and coordination environments of metal atoms[8–12], as well as specially engineered anchoring sites and various defects in the metal oxide support[13–17]. Therefore, these catalysts provide significant potential for addressing a myriad of challenges in catalysis. At the same time, the significant structural diversity of these catalysts poses

[1]Key Laboratory of Mesoscopic Chemistry of MOE, School of Chemistry and Chemical Engineering, Nanjing University, Nanjing, China. [2]Department of Chemistry, Zhejiang University, Hangzhou, China. [3]Key Laboratory of Excited-State Materials of Zhejiang Province, Zhejiang University, Hangzhou, China. [4]Key Laboratory of Surface and Interface Chemistry and Energy Catalysis of Anhui Higher Education Institutes, Department of Chemical Physics, University of Science and Technology of China, Hefei, China. [5]State Key Laboratory of Materials-Oriented Chemical Engineering, College of Chemical Engineering, Nanjing Tech University, Nanjing, China. [6]Hefei National Laboratory for Physical Sciences at the Microscale, University of Science and Technology of China, Hefei, China. [7]Institute of Zhejiang University-Quzhou, Quzhou, China. [8]State Key Laboratory of Separation Membranes and Membrane Processes, Tiangong University, Tianjin, China. [9]School of Chemical Engineering and Technology, Tiangong University, Tianjin, China. [10]Beijing National Laboratory for Molecular Sciences, New Cornerstone Science Laboratory, College of Chemistry and Molecular Engineering, Peking University, Beijing, China. [11]School of Chemistry and Chemical Engineering, Shanghai Jiao Tong University, Shanghai, China. [12]Jiangsu Key Laboratory of Vehicle Emissions Control, Nanjing University, Nanjing, China. [13]Frontiers Science Center for Critical Earth Material Cycling (FSC-CEMaC), Nanjing University, Nanjing, Jiangsu, China. [14]These authors contributed equally: Yujie Wen, Fang Wang. ✉e-mail: junchaochen@sjtu.edu.cn; luming@nju.edu.cn

substantial characterization challenges, creating difficulties in establishing structure-activity relationships, which are the basis for the rational design of better catalysts. For example, in single-atom Pt/CeO_2 catalysts, which often serve as model systems[18–20] and are widely studied for their applications in environmental contaminant removal and energy conversion[21–24], Pt sites can undergo dynamic transformations, maintaining their single-atom status while evolving into diverse structures with distinct catalytic properties under controlled atmospheres and/or annealing temperatures[21,25–27]. Current characterization techniques, such as aberration-corrected scanning transmission electron microscopy and X-ray absorption fine structure (XAFS)[28,29], primarily focus on the metal sites, probing the isolated states of individual metal atoms, their oxidation states and coordination numbers, while falling short of capturing the detailed local coordination environment around the metal atoms[30]. This environment, which includes not only the metal sites but also the surrounding atoms (e.g., coordinating species and coordination geometry), fundamentally dictates catalytic performance yet remains ambiguous[6,31]. Therefore, in order to fully elucidate the structure-activity relationship of oxide-supported SACs, developing high-resolution analytical techniques is urgently required.

Solid-state nuclear magnetic resonance (NMR) plays an indispensable role in investigating the structure and properties of materials across a wide variety of applications[32–35]. In particular, rich information has been obtained by applying ^{17}O NMR spectroscopy for oxygen-containing catalysts, taking advantage of the large ^{17}O chemical shift range (>1000 ppm)[36–39]. More recently, with the assistance of surface-selective ^{17}O labeling and DFT calculations, ^{17}O NMR has been successfully employed to distinguish oxygen sites at different surface layers and facets of oxide nanomaterials, and explore gas adsorption sites and gas-surface interactions[40–43]. However, there have been very few ^{17}O NMR studies on the structure of the supported catalysts[44,45], especially the important noble-metal-based catalysts, a key category of catalysts where single-atom dispersion is desired to reduce costs, not to mention structure-activity relationships. Here, we developed an approach based on ^{17}O solid-state NMR spectroscopy and DFT calculations, to reveal the detailed local structures of oxide-supported SACs, using Pt_1/CeO_2 as a model system. The precise structural information and reaction mechanisms obtained shed light on the factors responsible for the different CO oxidation performances of two Pt/CeO_2 SACs.

Results

Traditional characterization

An impregnation method (see Methods for details) was used to prepare the parent oxidized Pt cluster catalyst (denoted as Pt_nO_x/CeO_2, *vide infra*) using CeO_2 nanoparticles as the support which expose the thermodynamically stable (111) facets as determined by high-resolution transmission electron microscopy (HRTEM) (Supplementary Fig. 1a) and ^{17}O solid-state NMR (Supplementary Fig. 2). The high-angle annular dark-field scanning transmission electron microscopy (HAADF-STEM) image shows obvious Pt clusters (blue circles) on the surface with a diameter of approximately 5 nm (Fig. 1a). Pt_nO_x/CeO_2 was treated with 8.4 vol.% $H_2O(g)/Ar$ at 750 °C for 9 h, during which no further sintering occurred (Supplementary Figs. 1c and 3). Only isolated Pt atoms (orange circles) are observed in the HAADF-STEM image of the resulting material (Fig. 1a). The Pt single atoms turn out to be embedded in the CeO_2 lattice with a low-coordination number and the material is therefore denoted as Pt_{LC}/CeO_2 (LC for low-coordinated, *vide infra*). For a clearer illustration of the structure-activity

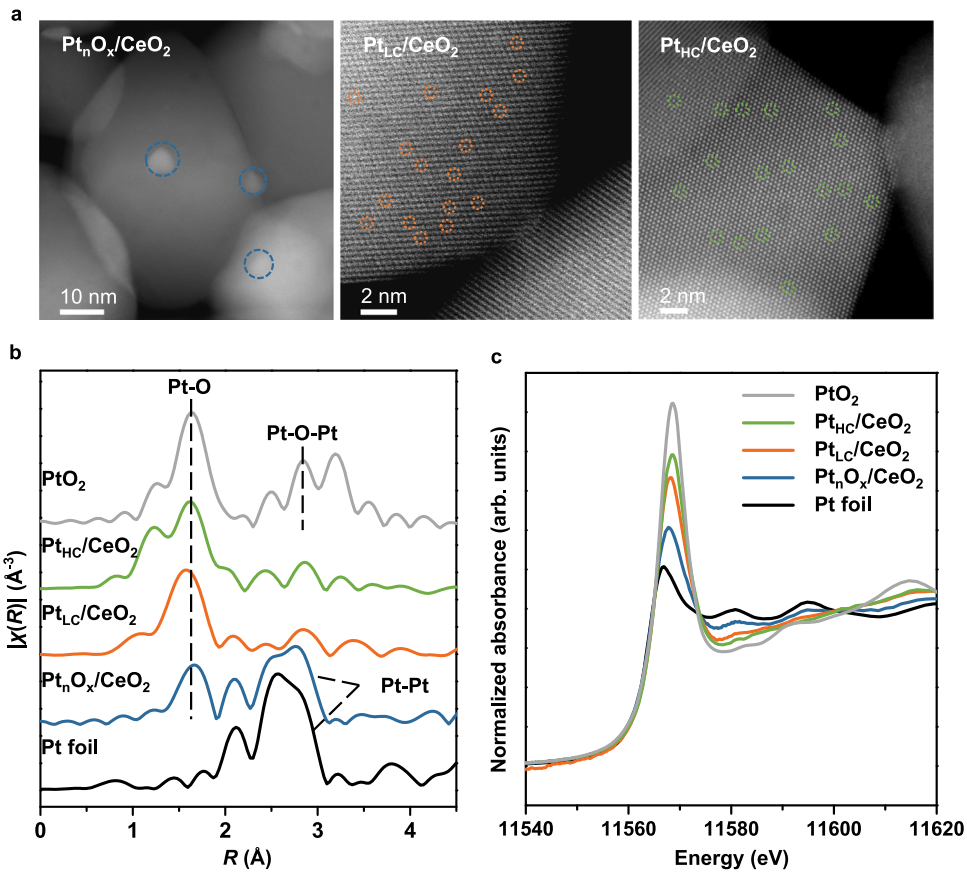

Fig. 1 | Electron microscopy and Structural characterization. a HAADF-STEM images for Pt_nO_x/CeO_2, Pt_{LC}/CeO_2 and Pt_{HC}/CeO_2. Blue circles highlight the Pt_nO_x cluster, while orange and green circles highlight single-atom Pt species in the SACs. **b** k^2-weighted Fourier-transformed EXAFS and **c** normalized Pt L_3-edge XANES spectra of Pt_nO_x/CeO_2, Pt_{LC}/CeO_2, Pt_{HC}/CeO_2, Pt foil and PtO_2.

https://doi.org/10.1038/s41467-025-58709-2

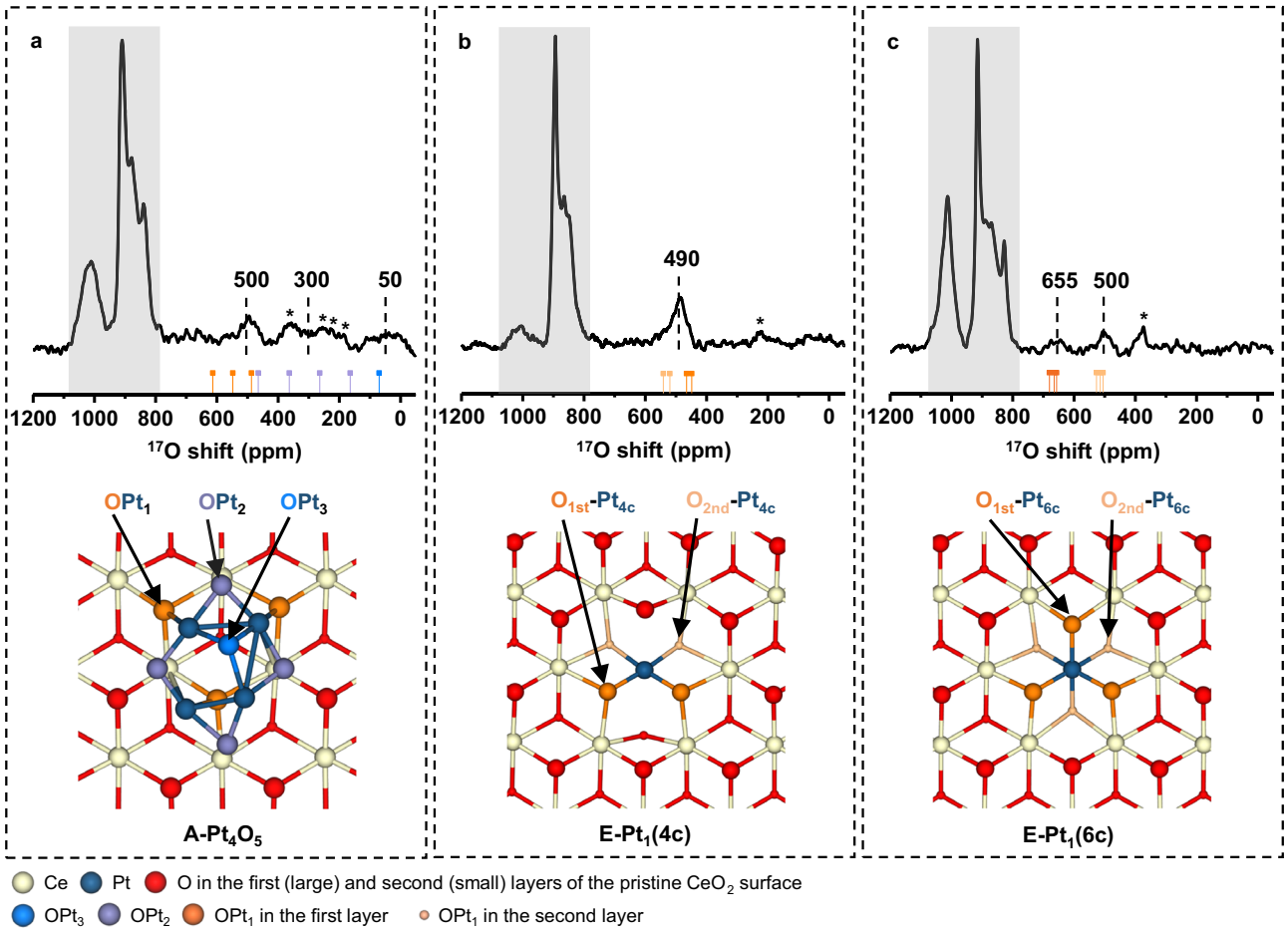

Fig. 2 | ^{17}O NMR data and surface structure. ^{17}O solid-state NMR spectra of (**a**) Pt_nO_x/CeO_2, (**b**) Pt_{LC}/CeO_2, and (**c**) Pt_{HC}/CeO_2 and the summary of calculated NMR shifts (center of gravities) of O atoms connected directly to Pt, as well as the corresponding structures. The spectra were recorded at a spinning speed of 53 kHz with a recycle delay of 0.2 s at 14.1 T. A rotor synchronized Hahn-echo pulse sequence ($\pi/6$-τ-$\pi/3$-τ-acquisition) with ^{1}H decoupling was applied. Asterisks denote spinning sidebands.

relationship of SACs, we prepared Pt_{HC}/CeO_2 (HC for high-coordinated, *vide infra*), a CeO_2-nanoparticles-supported single atom Pt catalyst with a higher coordination number, by using a conventional atom trapping method, as reported previously[15,46].

For Pt_nO_x/CeO_2, the extended X-ray absorption fine structure (EXAFS) spectrum exhibits contributions from Pt-O at 1.6 Å as well as Pt-Pt environments ranging from 2.4 to 3.0 Å (Fig. 1b, Supplementary Fig. 4 and Supplementary Table 1). Normalized X-ray absorption near-edge structure (XANES) results indicate that the oxidation state of Pt in this material is higher than that in Pt foil (Fig. 1c)[47]. The two peaks at 72.9 and 72.0 eV in the Pt 4*f* X-ray photoelectron spectroscopy (XPS) data can be attributed to Pt^{2+} and Pt^{+}, respectively (Supplementary Fig. 5 and Supplementary Table 2)[48]. X-band electron paramagnetic resonance (EPR) spectra further confirm the presence of Pt^{+} (Supplementary Fig. 6)[49]. In addition, diffuse reflectance infrared Fourier-transform spectroscopy (DRIFTS) data shows only a CO adsorption band at 2093 cm^{-1}, which is typically associated with CO adsorption on ionic Pt species, in addition to a weaker band at 2170 cm^{-1} owing to CO in the gas phase (Supplementary Fig. 7). Similar CO-DRIFTS results have been previously observed on oxidized Pt clusters[50]. Therefore, the presence of oxidized Pt clusters on the surface of the sample can be confirmed.

The absence of the peak related to Pt-Pt in the EXAFS spectrum of Pt_{LC}/CeO_2 in Fig. 1b substantiates the primary presence of single Pt atoms, confirming the formation of a SAC along with the results of HAADF-STEM (Fig. 1a). Therefore, this water vapor treatment disperses the cluster catalyst into a single-atom Pt catalyst, which is similar to the dispersion of Cu nanoparticles into Cu single atoms with the assistance of water in a very recent study by Fan et al. [51]. The structural change from Pt_nO_x to Pt single atoms was observed using EXAFS (Supplementary Fig. 8). Notably, the EXAFS spectra of both Pt_{LC}/CeO_2 and Pt_{HC}/CeO_2 show exclusively Pt-O scattering (Fig. 1b), with Pt_{LC}/CeO_2 exhibiting a lower coordination number of 4.0 ± 0.3 and Pt_{HC}/CeO_2 a higher coordination number of 6.0 ± 0.5 (Supplementary Fig. 4 and Supplementary Table 1). XANES data shows that Pt in Pt_{LC}/CeO_2 has a significantly higher oxidation state than Pt_nO_x/CeO_2, but is slightly lower than Pt_{HC}/CeO_2 (Fig. 1c). Similar XPS and EPR spectra are observed for both SACs, which suggest the presence of only Pt^{2+} and higher oxidation states than Pt_nO_x/CeO_2 (Supplementary Figs. 5, 6, and Supplementary Table 2) as well as the low concentrations of Ov on their surface (Supplementary Figs. 6 and 9, and related discussion in Supplementary Information). Bands at 2093 cm^{-1} are observed in DRIFTS data, again corresponding to CO on the top of ionic Pt species (Supplementary Fig. 7)[12,21]. These results indicate that two SACs with different coordination numbers have been obtained.

Precise local environment determined by ^{17}O solid-state NMR

Since the precise local environment of these Pt/CeO_2 catalysts is crucial for their catalytic performances, we combine ^{17}O solid-state NMR spectroscopy and DFT calculations to extract detailed structural information. Strong resonances ranging from 790 to 1080 ppm can be observed for all three samples, which are attributed to the oxygen ions at the first, second, third surface layers and in the bulk part of CeO_2 (111) (Fig. 2)[40]. This confirms that the predominantly exposed crystal facets of CeO_2 remained unchanged after thermal treatment in

https://doi.org/10.1038/s41467-025-58709-2

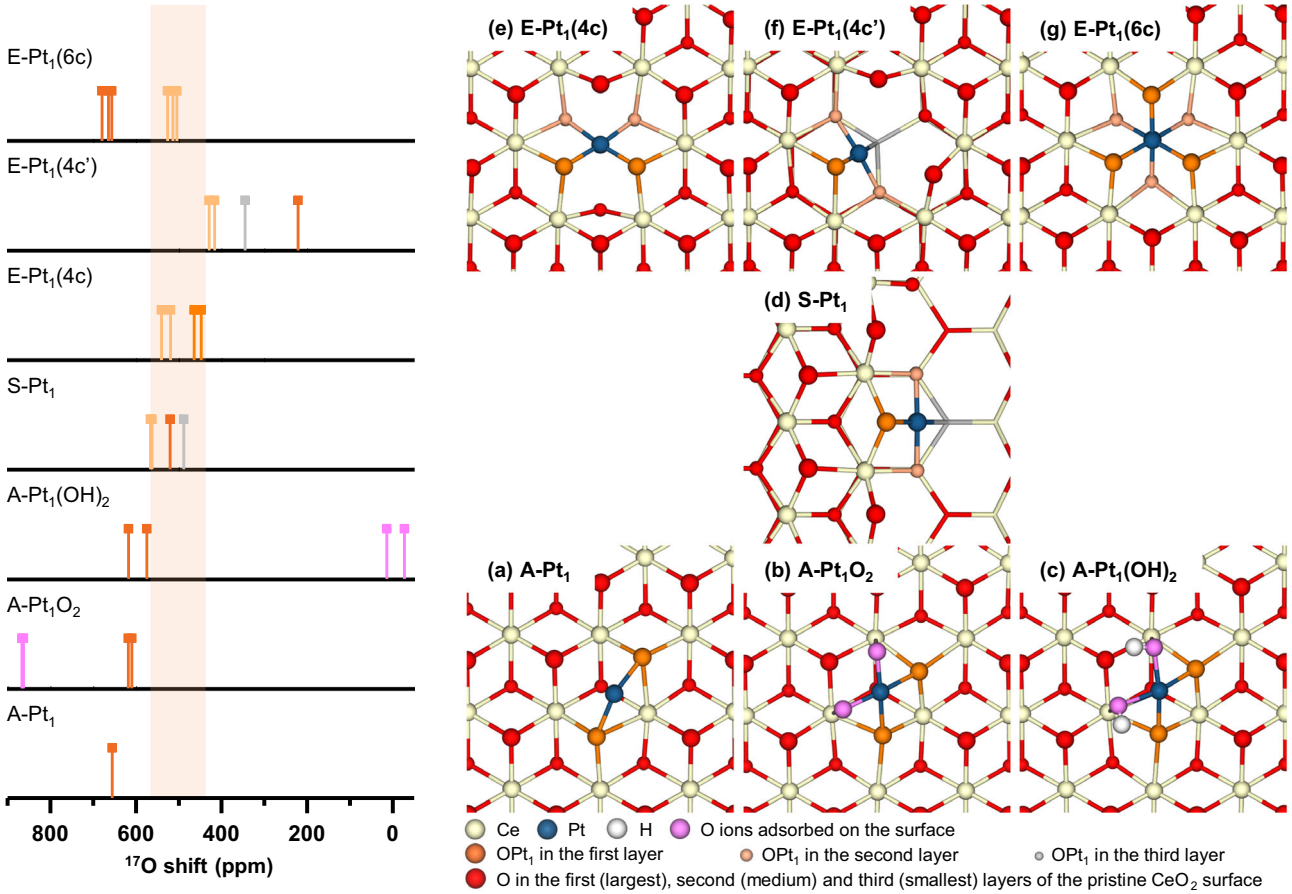

Fig. 3 | The summary of calculated NMR shifts of O atoms connected to Pt (left) using the potential models (right) of SACs. The light orange-marked area indicates the region where the new NMR signal corresponds to Pt_{LC}/CeO_2. The models include adsorbed Pt_1 species on the CeO_2 surface (A-Pt_1, A-Pt_1O_2 and A-$Pt_1(OH)_2$), Pt ions trapped in the steps of CeO_2 surface (S-Pt_1) and embedded Pt ions in the CeO_2 surface (E-Pt_1(4c), E-Pt_1(4c'), and E-Pt_1(6c)).

air or steam, consistent with observations in Supplementary Fig. 1. The major difference in NMR spectra is the signals at lower frequencies, which is expected considering the lower resonant frequencies of PtO_2 compared to CeO_2 (Supplementary Fig. 10). For Pt_nO_x/CeO_2 (Fig. 2a), three different sets of peaks are observed, centered at approximately 500, 300, and 50 ppm, respectively. The wide distribution of chemical shifts implies multiple binding modes between oxygen and the various Pt atoms in Pt_nO_x clusters. In contrast, the distribution of the ^{17}O NMR shifts in Pt_{LC}/CeO_2 and Pt_{HC}/CeO_2 is much narrower, suggesting more uniform oxygen environment in Pt-related sites in the two SACs (Fig. 2b, c). One relatively broad peak centered at 490 ppm, and two peaks centered at 500 and 655 ppm are observed for Pt_{LC}/CeO_2 and Pt_{HC}/CeO_2, respectively. At the same time, very different structures are expected for Pt_{LC}/CeO_2 and Pt_{HC}/CeO_2 due to their distinct NMR shifts.

DFT calculations of NMR parameters (i.e., isotropic chemical shift (δ_{iso}), quadrupolar coupling constant (C_Q), asymmetry parameter (η_Q), and center of gravity (δ_{CG})) were performed to assist the spectral assignments and extract more structural information of these catalysts. We use a model of adsorbed Pt_4O_5 cluster on CeO_2 (111) surface (denoted as A-Pt_4O_5) to represent Pt_nO_x/CeO_2 catalyst (see Supplementary Fig. 11 and additional discussion in the Supplementary Information). Oxygen ions connected to one, two and three Pt ions are associated with different NMR shifts and their calculated center of gravities (δ_{CG}s) follow the order: $OPt_1 > OPt_2 > OPt_3$ (see Fig. 2a, Supplementary Figs. 12–14, and Supplementary Tables 3–5). Thus, the signals centered at 500, 300, and 50 ppm obtained at 14.1 T can be assigned to OPt_1, OPt_2, and OPt_3, respectively. For SACs, several different structure models were developed, including the following possible Pt single atom structures (Fig. 3): different Pt_1 species adsorbed on CeO_2 (111) surface (denoted as A-Pt_1, A-Pt_1O_2, and A-$Pt_1(OH)_2$), Pt ion trapped into the CeO_2 (111) surface with steps (denoted as S-Pt_1)[14,46,52], and Pt ion embedded into the CeO_2 (111) surface with different coordination numbers (denoted as E-Pt_1(4c)[13], E-Pt_1(4c')[27,52], E-Pt_1(6c)[12,27,52]). Comparing the calculated NMR shifts (δ_{CG}s) for the oxygen ions directly connected to Pt (see Fig. 3, Supplementary Figs. 15–21 and Supplementary Tables 6–12, and related discussion in the Supplementary Information) to the experimental NMR spectrum of Pt_{LC}/CeO_2, only the models E-Pt_1(4c) and S-Pt_1 give rise to the peaks close to 490 ppm without additional peaks at other frequencies (also see Supplementary Figs. 22–27 and Supplementary Tables 13–18, and related discussion in the Supplementary Information). However, according to calculations, resonances with a relatively wide shift distribution in the range of 655–745 ppm are expected for oxygen ions (not connected to Pt) at the first and second layers in the model S-Pt_1 (Supplementary Fig. 28). The absence of such signals in the experimental NMR data confirms that Pt_{LC}/CeO_2 should be associated with the model E-Pt_1(4c). In this structure, a single Pt atom is trapped into the CeO_2 (111) surface, connecting to two O ions each from the first (δ_{CG}s ~ 478 ppm) and second surface layers (δ_{CG}s ~ 506 ppm), forming a square planar structure (Fig. 2b, Supplementary Fig. 19, and Supplementary Table 10). Furthermore, the experimental data obtained at three different external magnetic fields cannot be fitted with a single site (Supplementary Fig. 29, Supplementary Table 19 and related discussion in the Supplementary Information). Instead, two sites must be included in the fitting, further supporting the spectral assignments

https://doi.org/10.1038/s41467-025-58709-2

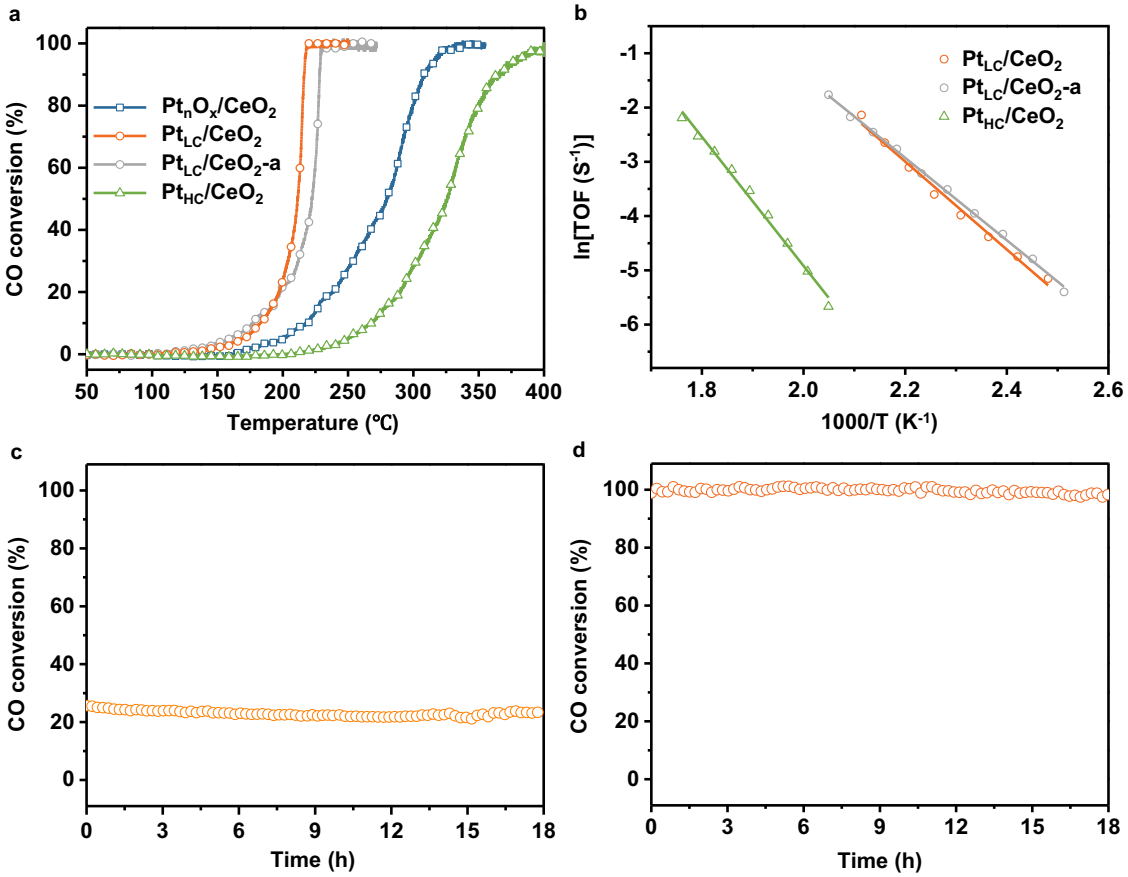

Fig. 4 | Catalytic performance. a The light-off curves for CO oxidation performances of Pt_nO_x/CeO_2, Pt_{LC}/CeO_2, Pt_{LC}/CeO_2-a, and Pt_{HC}/CeO_2. **b** Reaction rates of catalysts as a function of reaction temperature. Pt_{LC}/CeO_2 (orange line and circles), Pt_{LC}/CeO_2-a (grey line and circles) and Pt_{HC}/CeO_2 (green line and triangles). CO oxidation durability tests for Pt_{LC}/CeO_2 at (**c**) 200 °C and (**d**) 230 °C.

(Supplementary Fig. 30 and Supplementary Table 20 and related discussion in the Supplementary Information). The embedded Pt atoms are expected to contribute to the excellent thermal stability of Pt_{LC}/CeO_2. Similarly, only the calculated shifts from the model E-Pt_1(6c) are in agreement with the experimental NMR spectrum of Pt_{HC}/CeO_2, indicating a 6-coordinated Pt environment in this sample. The peaks at 655 and 500 ppm can be attributed to oxygen ions directly connected Pt (Pt-O-Ce) at the first and second layers, respectively (Fig. 2c, Supplementary Fig. 21 and Supplementary Table 12). The capability of ^{17}O NMR spectroscopy to distinguish a variety of different structures around Pt single atoms (Fig. 3) can be attributed to the fact that ^{17}O chemical shifts are dependent on atoms at the third coordination shell[42]. Therefore, the precise local environment, including coordination geometries, can be elucidated by combining ^{17}O NMR with DFT calculations, based on which an energetically feasible pathway for the dispersion process by water molecules was proposed (Supplementary Figs. 31 and 32, and related discussion in the Supplementary Information). Water molecules play a crucial role in dispersing platinum oxide clusters into single atoms on the support and in the final formation of the square planar structure of Pt species.

Structure-activity relationship

The Pt/CeO_2 catalysts were evaluated for CO oxidation and the light-off curves show that Pt_{LC}/CeO_2 demonstrates a marked improvement in catalysis compared to Pt_{HC}/CeO_2 (Fig. 4a). Notably, the onset temperature decreases from ~205 °C (Pt_{HC}/CeO_2, green line) to ~120 °C (Pt_{LC}/CeO_2, orange line) and the apparent activation energy becomes lower (Fig. 4b). A long-term duration test for Pt_{LC}/CeO_2 was also conducted at 200 and 230 °C, with CO conversion maintained at 23% and 100%, respectively, for at least 18 h (Fig. 4c, d). Furthermore, to investigate the thermal stability of Pt_{LC}/CeO_2, the catalyst was aged at 800 °C for an additional 24 h (denoted as Pt_{LC}/CeO_2-a, see Supplementary Figs. 3, 33, 34 and Supplementary Table 21, and related discussion in the Supplementary Information) and the catalytic performance for CO oxidation does not change much (Fig. 4a). These results indicate that the newly formed Pt_{LC}/CeO_2 possesses both high activity and thermal stability.

With detailed structures of the two SACs, the structure-activity relationship of the catalysts is explored. The CO oxidation process on Pt/CeO_2 is widely recognized to follow a Mars-van Krevelen (MvK) reaction mechanism[53]. Calculations show a CO adsorption energy of −2.09 eV at 4-coordinated Pt site in Pt_{LC}/CeO_2, and the following reaction between adsorbed CO and the vicinal bridging O only requires a minimal energy barrier of 0.10 eV (Fig. 5a). In contrast, the 6-coordinated Pt (Pt_{HC}/CeO_2) is associated with a much higher CO adsorption energy (−2.75 eV) (Fig. 5b). The difference in calculated CO adsorption energies for the two SACs is consistent with the in-situ CO-DRIFTS results (Supplementary Fig. 35), where CO molecules are found to be completely desorbed from Pt_{LC}/CeO_2 at 150 °C, whereas the Pt_{HC}/CeO_2 catalyst still exhibits strong adsorption at this temperature, suggesting the excessively strong bonding of CO on the Pt_{HC}/CeO_2 surface. Furthermore, a relatively high activation barrier of 1.10 eV needs to be overcome for adsorbed CO to react with the nearby surface lattice oxygen ion. This indicates that the surface of Pt_{HC}/CeO_2 is susceptible to poisoning by CO at low temperatures. Subsequently, an O_2 molecule fills the oxygen vacancy and the second CO molecule interacts with the adsorbed O_2 species, resulting in the formation of CO_2, which similar barriers are found in both catalysts. These data

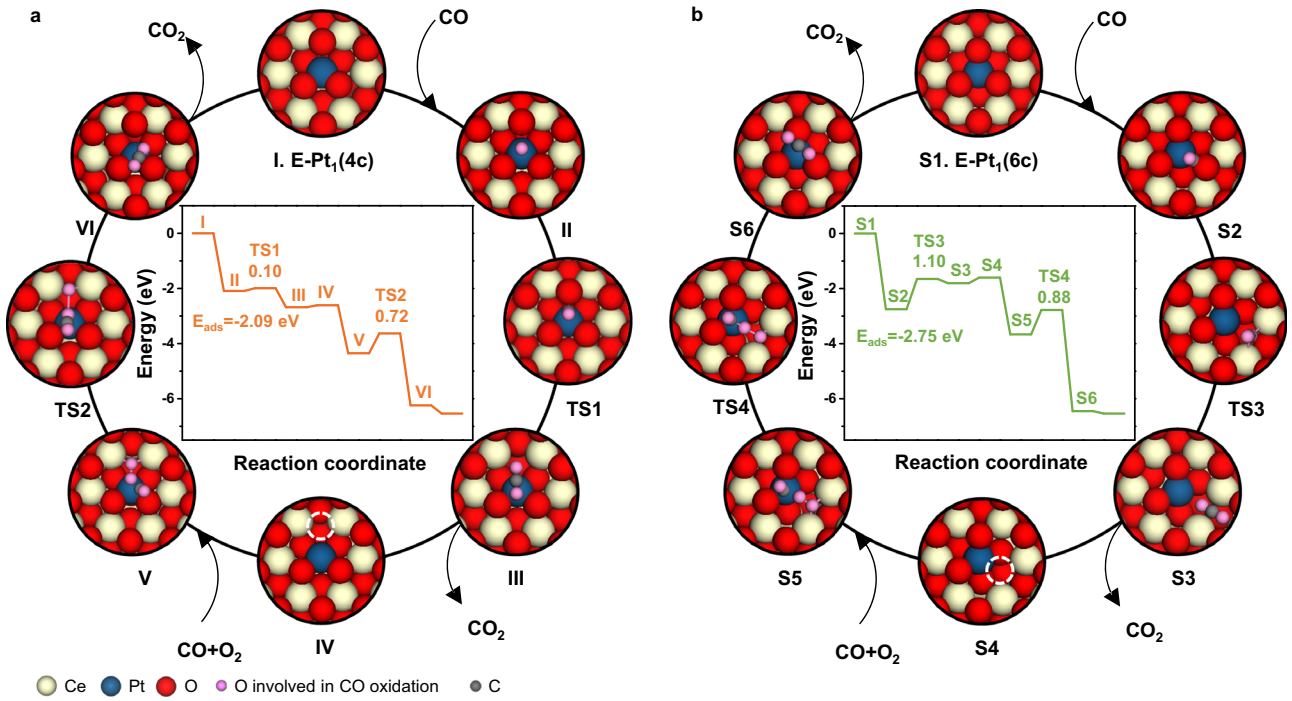

Fig. 5 | CO oxidation reaction mechanism. Calculated reaction pathways over (**a**) the model E-Pt_1(4c) and (**b**) the model E-Pt_1(6c). The insets show the calculated energy profiles and the structures of intermediates and transition states (TSs, see Supplementary Fig. 36 for details) of the key elementary steps.

show that the low-coordinated embedded single atoms in Pt_{LC}/CeO_2 are more effective as a CO oxidation catalyst than those with a higher coordination number in Pt_{HC}/CeO_2.

Discussion

We combine high-resolution ^{17}O solid-state NMR spectroscopy, along with DFT calculation, to reveal the precise local structure of ceria-supported Pt SACs, including coordination species and geometries, which is evidenced by characteristic ^{17}O NMR shifts. Owing to its very fine resolution, this method can resolve different Pt species including Pt clusters, and 4-and 6-coordinated Pt ions with unique geometries, thereby enabling the development of significantly improved structural models for DFT calculations of reaction mechanisms. On this basis, the enhanced performances of Pt_{LC}/CeO_2 can be ascribed to the square planar geometry of the Pt single atoms embedded into the ordered CeO_2 (111) surface, which is associated with moderately strong CO adsorption and low energy barriers. Our results demonstrate the establishment of structure-activity relationship of oxide-supported Pt SACs, highlighting the importance of extracting key local environment around single atoms for a better understanding of the properties of the catalysts and emphasizing that SACs require more detailed structural characterization. This method can also be extended to study other oxide-supported SACs, which have potential in solving critical challenges in sustainable development[3,4,54].

Methods

Synthesis of CeO_2 nanoparticles

$Ce(NO_3)_3{\cdot}6H_2O$ (99%; Sigma-Aldrich) was heated in air at 300 °C for 3 h to obtain CeO_2 nanoparticles (NPs).

Synthesis of Pt_nO_x/CeO_2

Pt_nO_x/CeO_2 was prepared by incipient wetness impregnation with $H_2PtCl_6{\cdot}6H_2O$ (≥37.50% Pt basis; Sigma-Aldrich) as the precursor. In a typical procedure, 1.0 g of CeO_2 NPs was slowly immersed in 0.5 mL of H_2PtCl_6 solution with a concentration of 0.02 g/mL, drop by drop. After drying overnight at 80 °C, the sample was calcined at 800 °C for 12 h in a tube furnace in dry air with a flow rate of 50 mL/min. The Pt content in the sample was determined by inductively coupled plasma atomic emission spectrometer (ICP-OES) to be 0.94 wt.%.

Synthesis of Pt_{LC}/CeO_2

The treatment was carried out in a fixed-bed reactor. 0.34 g of Pt_nO_x/CeO_2 sample (40–60 mesh) was packed into a U-type quartz tube and heated by programmable tube furnace from room temperature to 750 °C in Ar atmosphere with a flow rate of 50 mL/min. The whole stainless-steel gas path was kept at 90 °C. The sample was treated by 8.4 vol.% H_2O(g)/Ar at 750 °C for 9 h and then cooled down to 300 °C. Steam flow was discontinued and the sample was dried for an additional 2 h before cooling down to room temperature naturally. The obtained sample was denoted as Pt_{LC}/CeO_2. The Pt content in the sample was determined by ICP to be 0.92 wt.%.

Synthesis of Pt_{HC}/CeO_2

Pt_{HC}/CeO_2 was prepared using the conventional atom trapping method according to the literature[15,21]. In a typical procedure, 1.0 g of CeO_2 nanoparticle was immersed in 0.5 mL of H_2PtCl_6 solution with a concentration of 0.02 g/mL and the mixture was ground in a mortar. After drying overnight at 80 °C, the sample was calcined at 800 °C for 12 h in the muffle furnace. The Pt content in the sample was determined by ICP to be 0.97 wt.%.

Synthesis of CeO_2 Nanorods

The CeO_2 nanorods (NRs) were synthesized using the hydrothermal method. First, 0.868 g of $Ce(NO_3)_3{\cdot}6H_2O$ (Sigma-Aldrich, 99%) was dissolved in 10 mL of deionized water and stirred for 10 min. The solution was then mixed with 70 mL of aqueous NaOH (9 M), stirred for an additional 30 min, and transferred into a Teflon bottle. Subsequently, it was placed in a stainless-steel vessel autoclave and heated at 100 °C for 24 h in an oven. After cooling down to room temperature, a purple milky slurry was obtained. The precipitates were collected by centrifugation, washed three times with deionized water and ethanol, and then dried at 60 °C overnight. Finally, the powder was calcined in a tube furnace at 700 °C for 5 h in flowing air to obtain CeO_2 NRs.

Synthesis of Pt/CeO_2_S

Pt/CeO_2_S was prepared according to literature[21].

Basic characterization

The mass loading of Pt ions was determined by ICP-OES on an Optima 4300 DV spectrometer. X-ray photoelectron spectra (XPS) were recorded on a Thermo ESCALAB 250Xi instrument with Al Kα radiator (hν = 1486.6 eV). The binding energies were calibrated using C_{1s} at 284.8 eV. X-band EPR spectra were obtained at 107 K using a Bruker EMXplus spectrometer with the sample mass of 150 mg. Brunaure −Emmet−Teller (BET) specific surface area was measured by nitrogen adsorption at 77 K on a Micromeritics Tristar 2020 apparatus.

Electron microscopy

HRTEM images were acquired on a Talos F200X G2 TEM with an acceleration voltage of 200 kV. The aberration-corrected high-angle annular dark-field scanning transmission electron microscopy (HAADF-STEM) images were acquired on a FEI Titan G2 60–300 STEM equipped with a probe corrector and HF5000.

X-ray absorption fine structure (XAFS) spectroscopy

XANES and EXAFS data were conducted at the Pt L_3-edge on BL11B beamline at Shanghai Synchrotron Radiation Facility (SSRF), China, operated at 3.5 GeV with injection currents of 140–210 mA. A Si (111) double-crystal monochromator was used for the energy selection. The energy was calibrated by Pt foil (E_0 = 11564 eV). Pt foil and PtO_2 were used as reference samples and measured in the transmission mode. Other samples were measured in the fluorescence mode using a Lytle detector. XAS data were processed and analyzed using the Demeter software package[55].

Diffuse reflectance infrared Fourier transform spectroscopy (DRIFTS)

In-situ DRIFTS data of CO on catalysts were conducted on a VERTEX 70 spectrometer equipped with an in-situ Praying Mantis diffuse reflection reaction cell (Harrick Scientific) and a liquid nitrogen cooled mercury–cadmium–telluride (MCT) narrow-band detector with a resolution of 4 cm^{-1}. For each sample, about 30 mg Pt/CeO_2 was packed smoothly in the reaction cell and then pretreated with air for 1 h at 200 °C. After cooling to room temperature, the atmosphere was switched to argon for 10 min and the background spectra were recorded. Subsequently, the atmosphere was switched to 5 vol.% CO/Ar and CO-DRIFTS data were collected after allowing CO adsorption for 20 min. Then, the sample was purged with argon at room temperature for CO desorption until no further change could be observed in the spectra. Finally, while continuing the argon purge, the temperature was gradually increased to 160 °C at a rate of 2 °C/min. During the progress, spectra were collected to observe the temperature-dependent CO desorption behaviors from the catalysts.

^{17}O Isotopic Labeling

Samples (typically 150 mg) were put into a glass tube and heated at 120 °C under vacuum for 1 h to remove physically adsorbed water on the surface, then cooled to room temperature before $^{17}O_2$ gas (90% ^{17}O, Cambridge Isotope Laboratories) was introduced. The tube was sealed and heated at 270 °C for 24 h. This labeling temperature was carefully chosen such that surface enrichment of the interface sites (Pt-^{17}O-Ce) was optimized, balancing efficient labeling with minimal oxygen diffusion to ensure high ^{17}O concentration at the catalyst surface.

Solid-State NMR Measurement

^{17}O magic angle spinning nuclear magnetic resonance (MAS NMR) spectra were collected on a 9.4 T Bruker Avance III spectrometer at a Larmor frequency of 54.2 MHz with 1.3 mm HX and 3.2 mm HX MAS probes, a 14.1 T Bruker Avance III spectrometer at a Larmor frequency of 81.3 MHz with a 1.3 mm HX MAS probe, and a 20.0 T Bruker Avance NEO spectrometer at a Larmor frequency of 115.2 MHz with a 1.6 mm HX MAS probe. ^1H MAS NMR spectra were performed on a 9.4 T Bruker Avance III spectrometer at a Larmor frequency of 400 MHz with a 3.2 mm HX MAS probe. ^{17}O and ^1H chemical shifts are referenced to H_2O at 0.0 ppm and adamantane at 1.92 ppm, respectively. All samples were packed into laser marked rotors in a N_2 glove box. Dmfit package was used to simulate the ^{17}O NMR spectra.

CO Oxidation Performance

The CO oxidation reaction was performed in a fixed-bed reactor, with a gas mixture of 1 vol% CO and 8 vol% O_2 balanced with Ar at a total flow rate of 100 mL/min. Thirty milligrams of the catalyst with a particle size of 40–60 mesh, was diluted with inert SiC powder (0.3 g) to prevent the temperature gradients, was packed into a U-type quartz tube and pretreated with 10 vol% O_2/Ar at 300 °C for 1 h. After cooling down to room temperature, reactant gas was introduced with the temperature ramped at 2 °C/min until 450 °C. The concentration of outlet gas composition was monitored by on-line MS and the conversion of CO was determined by the concentration of outlet CO_2. The turnover frequency is calculated by using formula reported in ref. 46.

Flow rate of CO: 100 mL/min × 1 vol.% = 1 mL /min = 6.82×10^{-7} mol/s

$$\mathrm{TOF}\left(s^{-1}\right) = \frac{X_{CO} \times V_{CO}}{m_{catalyst} \times \frac{w_{Pt}}{M_{Pt}}} \quad (1)$$

where X_{CO} and V_{CO} are the CO conversion and the flow rate of CO (6.82×10^{-7} mol/s), respectively. $m_{catalyst}$ is the mass of catalysts (0.03 g). w_{Pt} is the weight percentage of Pt in catalysts determined by ICP-OES. M_{Pt} is the molar mass of Pt (195 g/mol).

DFT Calculation

Spin-polarized calculations were performed by using the *Vienna* Ab initio *Simulation Package* (*VASP*)[56], applying the generalized gradient approximation with the Perdew-Burke-Ernzerhof (PBE) functional[57]. To account for strong correlation effects, we implemented a Hubbard U correction[58], applying an effective U value of 5.0 eV to the localized Ce 4f orbitals. For all calculations, plane-wave kinetic energy cutoff was set at 500 eV[59]. Geometry optimizations were finished when the Hellman-Feynman force on each relaxed ion fell below 0.02 eV·$Å^{-1}$. The convergence thresholds were set at 10^{-5} eV for geometric optimizations and 10^{-8} eV for calculating chemical shifts and electric field gradients[40]. The van der Waals (vdW) interactions were incorporated by using Grimme et al.'s DFT-D3 method[60]. The optimized lattice parameter for cerium oxide is 5.448 Å, which is in agreement with the experimental value of 5.411 Å[61].

We used the CeO_2 (111) surface to model the CeO_2 substrate, consisting of six O−Ce−O trilayers with a (4 × 4) surface cell used in A-Pt_4O_5, A-Pt_9O_4, A-Pt_6O_7, S-Pt_1, E-Pt_1(4c), E-Pt_1(4c'), E-Pt_1(6c), E-Pt_1H_2 and A-Pt_3O_3, and a (3 × 3) surface cell used in A-Pt_1, A-Pt_1O_2, A-$Pt_1(OH)_2$, and A-Pt_3. A 2 × 2 × 1 Monkhorst-Pack grid was used to sample the k-point mesh. To eliminate slab-slab interactions, a 15 Å vacuum gap was introduced along the [111] direction.

The ^{17}O NMR parameter calculations were carried out in accordance with the methodology outlined in our previous work[40]. To calculate the quadrupolar parameters (C_Q and η_Q) for ^{17}O, the experimental quadrupole moment (Q) of −0.02558 barns[62] was used. The isotropic chemical shift (δ_{iso}) is defined as $\delta_{iso} = \delta_{ref} + \delta_{cal}$, where δ_{ref} is the reference chemical shift and δ_{cal} is the chemical shift value calculated using *VASP*. The δ_{ref} for each model was determined by aligning the average δ_{cal} of middle layers (O layers 4–9) to the experimental value of 877 ppm. All determined δ_{ref} values are in the range of 50–60 ppm (given in title of Supplementary Tables 3–13, 16 and 17).

For calculations of CO oxidation and Pt_4O_5 cluster decomposition, a (4 × 4) CeO_2 (111) surface with three O–Ce–O trilayers was used to model the substrate and the bottom CeO_2 trilayers were fixed for the geometric optimizations. The transition states for the CO oxidation reaction over E-Pt_1(4c) and E-Pt_1(6c) models were determined by employing the climbing-image nudged elastic band technique[63]. Further frequency calculations were performed to confirm the obtained TS structures.

The adsorption energies (E_{ads}) of H_2O and CO were calculated as follows:

$$E_{ads} = E_{adsorbate/slab} - E_{adsorbate} - E_{slab} \quad (2)$$

where $E_{adsorbate/slab}$ is the total energy of the adsorption complex, E_{slab} is the energy of the Pt/CeO_2 substrate, and $E_{adsorbate}$ is the energy of the gas-phase molecule.

The Gibbs free energy change for the dissociative water adsorption process of Pt_4O_5/CeO_2 were calculated as follows:

$$\Delta G = E_{abs} + \Delta E_{ZPE} - T\Delta S + \Delta U(0 \rightarrow T) \quad (3)$$

where E_{abs}, ΔE_{ZPE}, and ΔS are the adsorption energy of intermediate, change in zero-point energy and entropy change of the reaction, respectively. ΔU is the internal energy difference between 0 K and T. The thermal correction for adsorbate was calculated by using the *VASPKIT* package[64].

Data availability

The authors declare that the data generated in this study are provided in the Supplementary Information/Source Data files. Source data are provided with this paper.

References

1. Qiao, B. et al. Single-atom catalysis of CO oxidation using Pt_1/FeO_x. *Nat. Chem.* **3**, 634–641 (2011).
2. Yang, X.-F. et al. Single-atom catalysts: a new frontier in heterogeneous catalysis. *Acc. Chem. Res.* **46**, 1740–1748 (2013).
3. Liu, L. & Corma, A. Metal catalysts for heterogeneous catalysis: from single atoms to nanoclusters and nanoparticles. *Chem. Rev.* **118**, 4981–5079 (2018).
4. Lang, R. et al. Single-atom catalysts based on the metal-oxide interaction. *Chem. Rev.* **120**, 11986–12043 (2020).
5. Li, Z. et al. Well-defined materials for heterogeneous catalysis: from nanoparticles to isolated single-atom sites. *Chem. Rev.* **120**, 623–682 (2020).
6. Kaiser, S. K. et al. Single-atom catalysts across the periodic table. *Chem. Rev.* **120**, 11703–11809 (2020).
7. Ji, S. et al. Chemical synthesis of single atomic site catalysts. *Chem. Rev.* **120**, 11900–11955 (2020).
8. Yang, M. et al. Catalytically active Au-$O(OH)_x$- species stabilized by alkali ions on zeolites and mesoporous oxides. *Science* **346**, 1498–1501 (2014).
9. Liu, J. Catalysis by supported single metal atoms. *ACS Catal.* **7**, 34–59 (2017).
10. Ma, Y. et al. Tailoring of the proximity of platinum single atoms on CeO_2 using phosphorus boosts the hydrogenation activity. *ACS Catal.* **9**, 8404–8412 (2019).
11. Qin, R. et al. Surface coordination chemistry of atomically dispersed metal catalysts. *Chem. Rev.* **120**, 11810–11899 (2020).
12. Zhang, Z. et al. Memory-dictated dynamics of single-atom Pt on CeO_2 for CO oxidation. *Nat. Commun.* **14**, 2664 (2023).
13. Bruix, A. et al. Maximum noble-metal efficiency in catalytic materials: atomically dispersed surface platinum. *Angew. Chem. Int. Ed.* **53**, 10525–10530 (2014).
14. Dvorák, F. et al. Creating single-atom Pt-ceria catalysts by surface step decoration. *Nat. Commun.* **7**, 10801 (2016).
15. Jones, J. et al. Thermally stable single-atom platinum-on-ceria catalysts via atom trapping. *Science* **353**, 150–154 (2016).
16. Liu, P. et al. Photochemical route for synthesizing atomically dispersed palladium catalysts. *Science* **352**, 797–801 (2016).
17. Wan, W. et al. Highly stable and reactive platinum single atoms on oxygen plasma-functionalized CeO_2 surfaces: nanostructuring and peroxo effects. *Angew. Chem. Int. Ed.* **61**, e202112640 (2022).
18. Slavinskaya, E. M. et al. States of Pt/CeO_2 catalysts for CO oxidation below room temperature. *J. Catal.* **421**, 285–299 (2023).
19. Resasco, J. et al. Uniformity is key in defining structure–function relationships for atomically dispersed metal catalysts: the case of Pt/CeO_2. *J. Am. Chem. Soc.* **142**, 169–184 (2020).
20. Kottwitz, M. et al. Local structure and electronic state of atomically dispersed Pt supported on nanosized CeO_2. *ACS Catal.* **9**, 8738–8748 (2019).
21. Nie, L. et al. Activation of surface lattice oxygen in single-atom Pt/CeO_2 for low-temperature CO oxidation. *Science* **358**, 1419–1423 (2017).
22. Chen, L.-N. et al. Efficient hydrogen production from methanol using a single-site Pt_1/CeO_2 catalyst. *J. Am. Chem. Soc.* **141**, 17995–17999 (2019).
23. Jiang, Z. et al. Stabilizing platinum atoms on CeO_2 oxygen vacancies by metal-support interaction induced interface distortion: mechanism and application. *Appl. Catal. B* **278**, 119304 (2020).
24. Zhang, S. et al. Insights into the mechanism of n-Hexane reforming over a single-site platinum catalyst. *J. Am. Chem. Soc.* **142**, 16533–16537 (2020).
25. DeRita, L. et al. Structural evolution of atomically dispersed Pt catalysts dictates reactivity. *Nat. Mater.* **18**, 746–751 (2019).
26. Tan, W. et al. Fine-tuned local coordination environment of Pt single atoms on ceria controls catalytic reactivity. *Nat. Commun.* **13**, 7070 (2022).
27. Ding, C. et al. Reversible transformation and distribution determination of diverse Pt single-atom species. *J. Am. Chem. Soc.* **145**, 2523–2531 (2023).
28. Tieu, P. et al. Directly probing the local coordination, charge state, and stability of single atom catalysts by advanced electron microscopy: a review. *Small* **17**, 2006482 (2021).
29. Chen, Z. et al. Structural analysis of single-atom catalysts by X-ray absorption spectroscopy. *Acc. Chem. Res.* **57**, 521–532 (2024).
30. Wang, A. et al. Heterogeneous single-atom catalysis. *Nat. Rev. Chem.* **2**, 65–81 (2018).
31. Hülsey, M. J. et al. Approaching molecular definition on oxide-supported single-atom catalysts. *Acc. Chem. Res.* **56**, 561–572 (2023).
32. Zhang, W. et al. In situ solid-state NMR for heterogeneous catalysis: a joint experimental and theoretical approach. *Chem. Soc. Rev.* **41**, 192–210 (2012).
33. Ashbrook, S. E. et al. Recent advances in solid-state nuclear magnetic resonance spectroscopy. *Annu. Rev. Anal. Chem.* **11**, 485–508 (2018).
34. Xu, J. et al. Metal active sites and their catalytic functions in zeolites: insights from solid-state NMR spectroscopy. *Acc. Chem. Res.* **52**, 2179–2189 (2019).
35. Reif, B. et al. Solid-state NMR spectroscopy. *Nat. Rev. Method Prime* **1**, 2 (2021).
36. Peng, L. et al. Detection of Brønsted acid sites in zeolite HY with high-field ^{17}O-MAS-NMR techniques. *Nat. Mater.* **4**, 216–219 (2005).
37. Huo, H. et al. Solid-state MAS NMR studies of Brønsted acid sites in zeolite H-Mordenite. *J. Am. Chem. Soc.* **134**, 9708–9720 (2012).
38. Ashbrook, S. E. & Smith, M. E. Solid state ^{17}O NMR—an introduction to the background principles and applications to inorganic materials. *Chem. Soc. Rev.* **35**, 718–735 (2006).

39. Ashbrook, S. E. et al. ^{17}O NMR spectroscopy of crystalline microporous materials. *Chem. Sci.* **12**, 5016–5036 (2021).
40. Wang, M. et al. Identification of different oxygen species in oxide nanostructures with ^{17}O solid-state NMR spectroscopy. *Sci. Adv.* **1**, e1400133 (2015).
41. Wang, Q. et al. Mapping the oxygen structure of γ-Al_2O_3 by high-field solid-state NMR spectroscopy. *Nat. Commun.* **11**, 3620 (2020).
42. Chen, J. et al. Emerging applications of ^{17}O solid-state NMR spectroscopy for catalytic oxides. *ACS Catal.* **13**, 3485–3500 (2023).
43. Li, Y. et al. Distinguishing faceted oxide nanocrystals with ^{17}O solid-state NMR spectroscopy. *Nat. Commun.* **8**, 581 (2017).
44. Merle, N. et al. ^{17}O NMR gives unprecedented insights into the structure of supported catalysts and their interaction with the silica carrier. *J. Am. Chem. Soc.* **134**, 9263–9275 (2012).
45. Hope, M. A. et al. A ^{17}O paramagnetic NMR study of Sm_2O_3, Eu_2O_3, and Sm/Eu-substituted CeO_2. *Solid State Nucl. Magn. Reson.* **102**, 21–30 (2019).
46. Kunwar, D. et al. Stabilizing high metal loadings of thermally stable platinum single atoms on an industrial catalyst support. *ACS Catal.* **9**, 3978–3990 (2019).
47. Yoshida, H. et al. XANES study of the support effect on the state of platinum catalysts. *J. Synchrotron Radiat.* **6**, 471–473 (1999).
48. Lykhach, Y. et al. Reactivity of atomically dispersed Pt^{2+} species towards H_2: model Pt-CeO_2 fuel cell catalyst. *Phys. Chem. Chem. Phys.* **18**, 7672–7679 (2016).
49. Hejazi, S. et al. On the controlled loading of single platinum atoms as a Co-catalyst on TiO_2 anatase for optimized photocatalytic H_2 generation. *Adv. Mater.* **32**, 1908505 (2020).
50. Pereira-Hernández, X. I. et al. Tuning Pt-CeO_2 interactions by high-temperature vapor-phase synthesis for improved reducibility of lattice oxygen. *Nat. Commun.* **10**, 1358 (2019).
51. Fan, Y. et al. Water-assisted oxidative redispersion of Cu particles through formation of Cu hydroxide at room temperature. *Nat. Commun.* **15**, 3046 (2024).
52. Su, Y.-Q. et al. Theoretical approach to predict the stability of supported single-atom catalysts. *ACS Catal.* **9**, 3289–3297 (2019).
53. Beniya, A. & Higashi, S. Towards dense single-atom catalysts for future automotive applications. *Nat. Catal.* **2**, 590–602 (2019).
54. He, C. et al. Recent advances in the catalytic oxidation of volatile organic compounds: a review based on pollutant sorts and sources. *Chem. Rev.* **119**, 4471–4568 (2019).
55. Ravel, B. & Newville, M. *ATHENA, ARTEMIS, HEPHAESTUS*: data analysis for X-ray absorption spectroscopy using *IFEFFIT*. *J. Synchrotron Radiat.* **12**, 537–541 (2005).
56. Kresse, G. & Hafner, J. Ab Initio molecular-dynamics simulation of the liquid-metal-amorphous-semiconductor transition in germanium. *Phys. Rev. B* **49**, 14251–14269 (1994).
57. Perdew, J. P. et al. Generalized gradient approximation made simple. *Phys. Rev. Lett.* **77**, 3865–3868 (1996).
58. Nolan, M. et al. The electronic structure of oxygen vacancy defects at the low index surfaces of ceria. *Surf. Sci.* **595**, 223–232 (2005).
59. Blöchl, P. E. Projector augmented-wave method. *Phys. Rev. B* **50**, 17953–17979 (1994).
60. Grimme, S. et al. A consistent and accurate ab initio parametrization of density functional dispersion correction (DFT-D) for the 94 elements H-Pu. *J. Chem. Phys.* **132**, 154104 (2010).
61. Kümmerle, E. A. & Heger, G. The structures of C–$Ce_2O_{3+\delta}$, Ce_7O_{12}, and $Ce_{11}O_{20}$. *J. Solid State Chem.* **147**, 485–500 (1999).
62. Sundholm, D. & Olsen, J. Finite element multiconfiguration Hartree-Fock calculations on carbon, oxygen, and neon: the nuclear quadrupole moments of ^{11}C, ^{17}O, and ^{21}. *Ne. J. Phys. Chem.* **96**, 627–630 (1992).
63. Henkelman, G. et al. A climbing image nudged elastic band method for finding saddle points and minimum energy paths. *J. Chem. Phys.* **113**, 9901–9904 (2000).
64. Wang, V. et al. VASPKIT: a user-friendly interface facilitating high-throughput computing and analysis using VASP code. *Comput. Phys. Commun.* **267**, 108033 (2021).

Acknowledgements

This work was supported by National Key R&D Program of China (Grant No. 2021YFA1502803) to L.P., the National Natural Science Foundation of China (NSFC) (Grant Nos. 22472075, 22272075, W2421041, 21972066, and 91745202) to L.P., NSFC—Royal Society Joint Program (Grant No. 21661130149) to L.P., the NSFC (Grant Nos. 21773047 and U1832180) to Z.Z., Zhejiang Provincial Natural Science Foundation (ZJNSF) (Grant No. LGC22B050025) to H.G., and the NSFC (Grant No. 22402119) to J.C.L.P. thanks the Royal Society and Newton Fund for a Royal Society—Newton Advanced Fellowship. This work was also supported by the Research Funds for the Frontiers Science Center for Critical Earth Material Cycling, Nanjing University, and a Project Funded by the Priority Academic Program Development of Jiangsu Higher Education Institutions. We thank the BL11B station in the Shanghai Synchrotron Radiation Facility (SSRF). We thank Prof. Arno P.M. Kentgens and Dr. Ernst R.H. van Eck in the Radboud University for invaluable discussions and help in this work. We are grateful to the High Performance Computing Center of Nanjing University for doing the numerical calculations in this paper on its blade cluster system.

Author contributions

Y.W., J.C., J.Z., X.K., H.G., and L.P. performed ^{17}O isotope enrichment, collected as well as analyzed the NMR spectra; Y.W., Q.W., X.X., J.W., J.-H.D., and M.W. conducted other characterizations of the catalysts and analyzed the results; Y.W., C.D., and L.N. carried out the preparation of SACs and the reaction performance; F.W. and W.L. conducted the DFT calculations; Z.Z., W.H., W.T., and W.D. provided valuable suggestions; L.P. conceived the idea, designed the study and coordinated the project. Y.W., J.C., and L.P. wrote the manuscript, and all authors discussed the experiments and final manuscript.

Competing interests

The authors declare no competing interest.

Additional information

Supplementary information The online version contains supplementary material available at https://doi.org/10.1038/s41467-025-58709-2.

Correspondence and requests for materials should be addressed to Junchao Chen or Luming Peng.

Peer review information *Nature Communications* thanks Olga Lapina, Talat Shahnaz Rahman, and the other, anonymous, reviewer(s) for their contribution to the peer review of this work. A peer review file is available.